Geophysical Journal International

Geophys. J. Int. (2024) **236,** 1–13
Advance Access publication 2023 October 19
GJI Seismology

https://doi.org/10.1093/gji/ggad405

Crustal and uppermost mantle structure near the Gloria Fault, North Atlantic, from ocean bottom seismometer surface wave observations

Juan I. Pinzón [1], Susana Custódio,[1] Graça Silveira [1,2] Frank Krüger,[3] João Mata[1] and Luis Matias[1]

[1] *Instituto Dom Luiz (IDL), Faculdade de Ciências, Universidade de Lisboa, Lisbon,* 45158*, Portugal. E-mail: juan.pinzon@academicos.udg.mx*
[2] *Departamento de Física, Instituto Superior de Engenharia de Lisboa (ISEL), Lisbon,* 1959-007*, Portugal*
[3] *Institute of Geosciences, University of Potsdam, Potsdam,*14476*, Germany*

Accepted 2023 October 1. Received 2023 September 20; in original form 2022 December 21

SUMMARY

In this work, we present both 1-D and 3-D shear wave velocity (*Vs*) models of the oceanic crust and uppermost mantle below the Deep OCean Test ARray area, located ∼ 70 km north of the central section of the Gloria Fault, in the eastern North-Atlantic Ocean. The velocity models are inferred from the dispersion of surface waves recorded on ocean bottom seismometers. Dispersion measurements are obtained from the analysis of ambient seismic noise at short periods (< 14 s) and teleseismic surface waves at long periods (> 14 s) using the two-station method. The 1-D *Vs* model is inferred from the joint inversion of Rayleigh wave phase velocities and Love wave group and phase velocities. The 3-D tomographic model is obtained by inversion of 2-D Love wave group velocity maps as a function of depth, further constrained by the average of Love wave phase velocities obtained from ambient noise (4–9 s) and the average Rayleigh and Love wave phase velocities calculated from teleseismic data (14–44 s).

The 1-D *Vs* model shows a sediment layer with a low velocity of 1.05 km s^{-1}, similar to previous studies in the region. Below the sediments, we find an oceanic crust with velocities ranging from 3.3 to 4.5 km s^{-1}. The model reaches an unusually high velocity of 4.9 km s^{-1} in a 20 km thick layer at depths between 16 and 36 km. We interpret this fast velocity layer as indicative of the presence of harzburgite, a residue of enhanced melting that might have been formed by the proximity between the Mid-Atlantic Ridge and the Azores mantle plume. At greater depths the velocity decreases, forming a low-velocity zone that reaches a minimum at ∼ 70 km depth, which we interpret as the maximum depth for the lithosphere–asthenosphere boundary. The 3-D model shows a structure that is mostly horizontally layered, with *Vs* isocontours at 3.5–4.5 km s^{-1} highlighting oscillations of the crustal structure with wavelengths of ∼25–30 km. These oscillations may be due to changes in the rate of mantle upwelling and magma supply rate.

Key words: Seismic noise; Seismic tomography; Surface waves and free oscillations; Crustal structure.

1 INTRODUCTION

The Gloria Fault (GF) is a major oceanic strike-slip fault that separates the Eurasian and Nubian tectonic plates (Fig. 1). Locally, the plates move past each other at a rate of ∼5 mm yr^{-1} (Fernandes *et al.* 2003, 2006; DeMets *et al.* 2010). The GF extends from the Azores Plateau until the Madeira Tore Rise (MTR), reaching a length of ∼1000 km. Oceanic crust along the GF gets older from west to east, changing from ∼55 to ∼110 Ma in the Eurasian Plate and from ∼60 to ∼120 Ma in the Nubian Plate (Müller *et al.* 2008). During the last century, three major ($M \geq 7.0$) earthquakes occurred along the GF, all within one decade: $M_s = 7.1$ on 1931 May 20 and 7.1 on 1939 May 08; and $M_w = 8.3$ on 1941 November 25. A more recent $M_s = 7.9$ earthquake occurred on 1975 May 26 near to the GF, but on a fracture zone to its south (Udías *et al.* 1976; Buforn *et al.* 1988). The focal mechanisms of these earthquakes indicate mainly right-lateral strike-slip, in agreement with the regional tectonics, with the exception of the 1939 earthquake, which shows a dominantly normal solution, marking the transition to the extensional regime of the Azores (Fig. 1). Due to the distance of the GF to the continents and to the Azores islands, little is known about the low to moderate magnitude seismicity and the prevailing processes in the area. Still, understanding the structure and dominant processes of this region is key for earthquake and tsunami risk assessment.

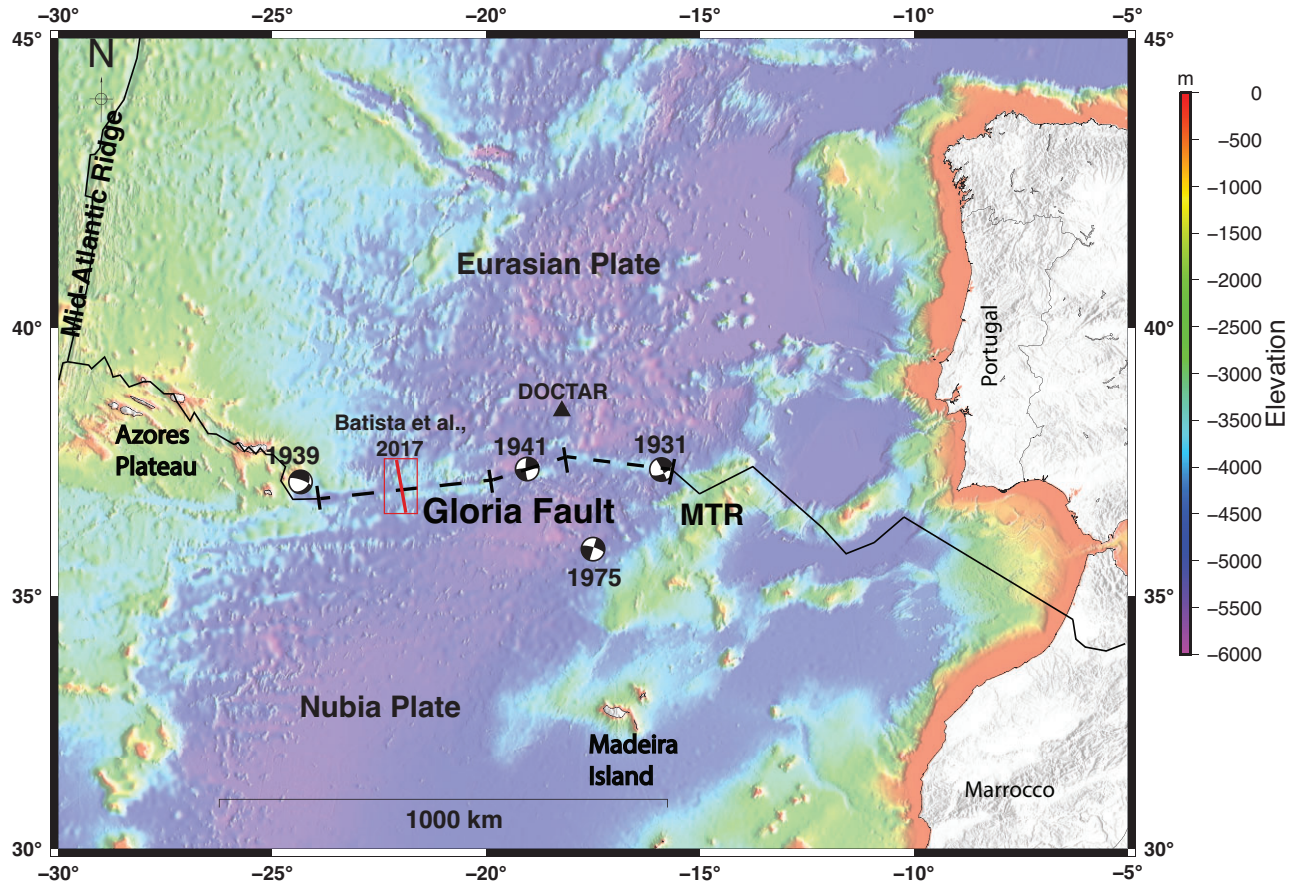

Figure 1. Map of the GF domain: the black dashed line denotes the GF, with an approximate length of ∼1000 km between the Azores triple junction (ATJ) to the west and the MTR to the east. Focal mechanisms are shown for the major ($M_w > 7$) instrumental earthquakes. The black triangle shows the location of the DOCTAR used in this work. The red line indicates the location of the seismic profile from Batista *et al.* (2017). The bathymetry was downloaded from GEBCO (www.gebco.net).

The oceanic crust has been classically described as horizontally stratified and fairly homogeneous laterally. Vertically, the classical structure comprises sediments, basalt lavas and gabbros, sequentially from the surface downwards (Raitt 1963; Penrose Conference participants 1972). However, recent studies have shown that oceanic crust can have important lateral variability indicative of its generation and evolution (e.g. White *et al.* 1992). The complexity of oceanic crustal accretion varies from place to place depending on genesis processes at mid-ocean ridges, which in turn depend on spreading rates, temperatures and compositions, among other (Dick *et al.* 2006; Olive 2023), as well as on subsequent deformation processes, often associated with fracturing and water circulation (Grevemeyer *et al.* 2018). In particular, lateral oscillations of oceanic crustal thickness found in profiles perpendicular to the Mid-Atlantic Ridge have been interpreted as indicative of temporal changes in mantle upwelling and flow (e.g. Pariso *et al.* 1995; Tucholke *et al.* 1997; Bonatti *et al.* 2003; Shinevar *et al.* 2019; Vaddineni *et al.* 2021).

Recent oceanic geophysical surveys have shed light into the previously poorly known region of the GF. Batista *et al.* (2017) carried out a seismic refraction and reflection study on the western segment of the GF (Fig. 1). Their results showed an oceanic crust with a thickness of ∼8.5 km. In addition, the authors found a 4 km thick complex layer of partially serpentinized mantle peridotite intruded by gabbros, representing a transition zone between the crust and the upper mantle. Hannemann *et al.* (2017) used ocean bottom seismometers (OBS) deployed within the scope of the Deep OCean Test ARray (DOCTAR, Fig. 1) to study the seismic structure at a location a bit further to the east than that studied by Batista *et al.* (2017). Using receiver functions, they imaged the Moho boundary at a shallower depth, between 5 and 8 km. In addition, they observed the lithosphere–asthenosphere boundary (LAB) at ∼70–80 km depth. From the analysis of *P*-wave polarization, Hannemann *et al.* (2016) inferred an increase in the thickness of the oceanic crust from ∼5 to ∼8 km towards the GF. They further observed a decrease in mantle *Vs* from ∼5.5 to ∼4.5 km s^{-1} at depths between 4 and 10 km, also towards the GF. They concluded that both the decrease in shear wave velocity and the increase in thickening towards the fault were related to deformation associated with the fault. Krüger *et al.* (2020) used three seismological arrays, located on the Madeira Island, mainland Portugal and the OBS DOCTAR, to detect 355 earthquakes in the eastern Mid-Atlantic with local magnitudes between −0.5 and 5.2 over a 10-month period, showing very high *Vso* ∼ 4.8 km s^{-1} for the uppermost mantle.

In this study, we further characterize the oceanic crust north of the GF by developing both a 1-D average vertical model and a full 3-D tomographic model that images both lateral and vertical structural variations in *S*-wave velocity (*Vs*). In Section 2, we briefly describe the DOCTAR OBS experiment, the data used and its pre-processing. In Section 3, we explain how we inferred empirical Green's functions (EGFs) from the analysis of ambient noise (Shapiro & Campillo 2004) and from teleseismic events using the

two-station method (Sato 1955; Soomro *et al.* 2016). The dispersion of surface waves is then measured from the EGFs. In Section 4, we invert the dispersion curves of surface waves in order to obtain both 1-D and 3-D *Vs* models of the shallow structure of the region. We obtain the 1-D velocity model by inverting the average of the Love wave group and phase velocities and the Rayleigh wave phase velocities. The 3-D *Vs* model is computed by inverting 2-D Love wave group velocity maps, complemented with the average of the Rayleigh and Love wave phase velocities. In Section 5, we discuss our results considering the current knowledge on the composition, structure and dynamics of the oceanic crust and uppermost mantle. Given the well-established interdependence between magma supply rates, crustal thickness, mantle potential temperatures, spreading rates and *Vs* (e.g. Dalton *et al.* 2014; Zhou *et al.* 2020), our study sheds light on the evolution of the mid-Atlantic ridge on the vicinity of the Azores between 75 and 85 Ma, emphasizing the consequences of the interplay between a plume and a slow-spreading ridge.

2 DATA PRE-PROCESSING

The DOCTAR OBS instruments were deployed ∼70 km north of the central section of the GF in the eastern North Atlantic Ocean, for a time interval of approximately 11 months between 2011 June and 2012 April (Hannemann *et al.* 2013). The deployment encompassed 12 broad-band OBSs with a maximum interstation distance of ∼73 km and average spacing between 10 and 20 km. Each OBS was equipped with a broad-band seismometer (Guralp CMG-40T, with a corner period of 60 s) and a hydrophone (HighTechInn HTI-04-PCA/ULF). The sampling rates of the seismometers and hydrophones were set to 100 Hz. The seismometer at station D05 was not used for this study because two of its components were jammed (vertical and one horizontal). However, its hydrophone was used, even though it failed a month before recovery. Furthermore, despite some technical problems and after careful inspection, the hydrophone of station D03 was only used for the noise analysis, but not for the analysis of the teleseismic events. The time correction and orientation of the horizontal components were previously performed for the DOCTAR data set by Hannemann *et al.* (2013). In our pre-processing of the data, we started by demeaning, detrending and deconvolving the instrumental response. Next, daily streams of data of the entire array were synchronized to the same starting and ending times. The recordings were then downsampled to 10 Hz to reduce computation time. Finally, we bandpass filtered the hydrophone and seismic data. For ambient noise analysis, we filtered the data between 0.25 and 25 s. For the analysis of teleseismic events, we used a longer period passband of 5–60 s. This pre-processing was applied to all four channels of the OBSs: vertical (Z), north–south (N), east–west (E) and hydrophone (H).

3 DISPERSION MEASUREMENTS

We measured the dispersion of surface waves recorded at DOCTAR sensors using both ambient seismic noise and teleseismic events. For the seismic ambient noise analysis, we computed EGFs by phase cross-correlation (PCC) of daily OBS streams followed by a time–frequency phase weighted stack (tf-PWS), as described in Schimmel *et al.* (2011). PCC is amplitude-unbiased and therefore requires no pre-processing, unlike the classical correlation method that requires normalization in the time-domain and spectral whitening (Bensen *et al.* 2007). We applied this methodology to data recorded on the three components of the seismometer (E, N, Z) as well as on the hydrophone (H). We then rotated NN and EE interstation cross-correlations to obtain the radial (RR) and transverse (TT) components. The acausal and causal sides of the daily cross-correlograms were truncated, reversed and stacked in order to improve the signal-to-noise ratio (SNR) and obtain the final EGFs, representative of the entire time interval of the deployment. Figs 2(b) and (c) show the results of the noise cross-correlation functions (NCF) of ambient noise as a function of distance for the hydrophone and the transverse components, respectively. Theoretically, we would expect the hydrophone to be dominated by the Rayleigh wave fundamental mode and the transverse component to be dominated by the Love wave fundamental mode. In oceanic environments, short-period Rayleigh waves are mostly sensitive to the water layer (e.g. Harmon *et al.* 2007; Yao *et al.* 2011; Carvalho et al 2022; Zhang *et al.* 2022). The NCF of the hydrophone shows a clear moveout time corresponding to a velocity of $\sim$1.3 km s^{-1}, which reflects the influence of the water on Rayleigh–Scholte waves at very short periods. The NCF of the transverse component shows a moveout time corresponding to a velocity of $\sim$3.3 km s^{-1}, related to the propagation of Love waves. Love waves are not influenced by the water layer as they only contain *SH*-wave energy, which only propagates in solids.

From the EGFs, we measured group velocity as a function of period using a multiple-filter technique (MFT, Dziewonski *et al.* 1969; Herrmann & Ammon 2002). Fig. 2(d) shows the result for station pair D09–D11, transverse component, which is dominated by the Love wave fundamental mode. The phase velocity dispersion was measured using the automated frequency–time analysis method of Levshin & Ritzwoller (2001).

We complemented the previous measurements with a classical two-station analysis, which uses the signal from distant high-magnitude earthquakes. This method was first introduced by Sato (1955) and decades later improved by Meier *et al.* (2004) and automated by Soomro *et al.* (2016). This methodology has been applied with success in several regional (e.g. Foster *et al.* 2013) and local studies (e.g. Bonadio *et al.* 2018; Carvalho *et al.* 2019). The two-station method reduces the influence of source parameter uncertainties and reduces the problem of the 2π ambiguity in phase velocity measurements due to the relatively small distances between stations (Soomro *et al.* 2016). For each pair of stations, the teleseismic records were cross-correlated, thus generating EGFs, from which the phase velocity could be measured. We initially selected 126 earthquakes with $M_w \geq 6.0$ for the analysis. After applying the cross-correlation, we could reliably measure phase-velocity dispersion curves for 32 teleseismic events in the hydrophone channel and 23 events in the vertical seismic component (Fig. 3a). Because the hydrophone channel displayed a higher SNR, we retained its results for further analysis. It was not possible to select any path that involved station D03, as this station's hydrophone did not work properly. For the transverse component, we could only reliably extract phase velocities for eight events, given the low SNR of the horizontal components. Figs 3(b) and (c) show all the measured phase velocity dispersion curves as a function of period, considering all earthquakes and all paths, together with the average phase velocity for the hydrophone and the transverse components of the seismometer.

Fig. 4 shows all the group and phase velocity dispersion curves successfully extracted from DOCTAR data. Ambient noise analysis yields measurements at short periods ($<$ 14 s), whereas the two-station method yields measurements at longer periods ($>$ 14 s). Love wave dispersion was measured from the analysis of transverse seismic data as usual, whereas Rayleigh wave phase velocities were

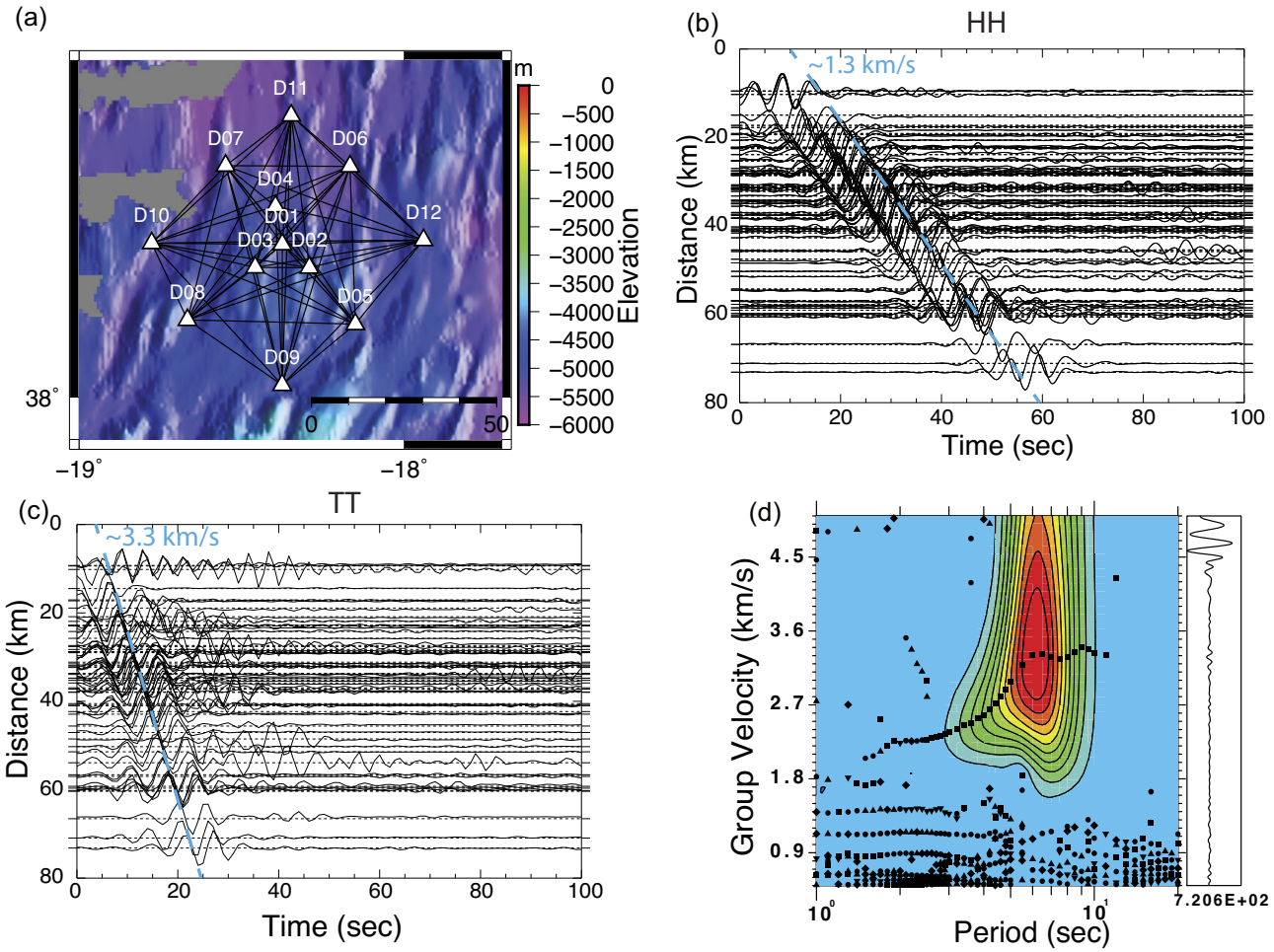

Figure 2. (a) Map of the DOCTAR experiment showing all paths between stations. The seismometer of station D05 (red triangle) was not used due to malfunctioning but the hydrophone was used. (b) and (c) EGF as a function of interstation distance for the hydrophone and the transverse components, respectively. The transverse component was further bandpass filtered between 4–25 s to observe more clearly the moveout of the Love wave. The blue lines correspond to velocities of ∼1.3 and ∼3.3 km s^{-1}s, respectively. (d) Example of a group velocity energy diagram on the transverse component for path D09–D11.

taken from hydrophone observations, which showed a higher SNR than the vertical and radial seismic components. As mentioned before, at short periods (<14 s) Rayleigh waves are strongly affected by the water layer and show a reduced sensitivity to the crustal structure. Therefore, in this period range we used only Love wave dispersion curves for the subsequent analysis. At longer periods (>14 s), we used both the Rayleigh and Love phase velocity measurements inferred from the two-station method. However, we avoided using the Rayleigh wave phase measurements from the two-station method for periods between 10 and 14 s, because in this interval the dispersion curves show a sharp increase related to the depth of the water layer. When only a few paths could be successfully retrieved, we used the average of the curves as representative of the general regional structure.

4 SHEAR WAVE VELOCITY ESTIMATION METHODS

4.1 Vertical (1-D) surface wave inversion

The estimation of a 1-D shear wave velocity model for the region is an important first step. In addition to the averaged information that it provides on the local Earth structure, the resulting model can be later used as an *a priori* reference model for the 3-D tomography. We used SURF96 (Herrmann 2013) to infer a 1-D shear wave velocity structure from the observed dispersion measurements by linearized least-squares inversion. At short periods, we used the average of the Love wave group velocities (3–9 s) and the average of the Love wave phase velocities (4–9 s), both inferred from ambient noise analysis. At longer periods, we used Love wave phase velocities (14–42 s) and Rayleigh wave phase velocities (15–44 s) inferred from teleseismic surface waves with the two-station method (see Fig. S1, Supporting Information and Table 1). The input surface wave velocity uncertainties were estimated as the standard error of the observations for each period.

We tested several simple starting models for the linearized inversion. They consisted of a half-space model, covered by a sediment and a water layers. In the study region, the water layer thickness varies from −4420 to −5283 m between stations. In the work presented here, we made the simplifying approximation that the water layer was 5 km, thus not accounting for lateral variations. We also assumed that the sediment layer had a thickness of 600 m, following the local conditions inferred by Hannemann *et al.* (2016). Below the sediments, we used 10 layers of 1 km thickness, followed by layers of

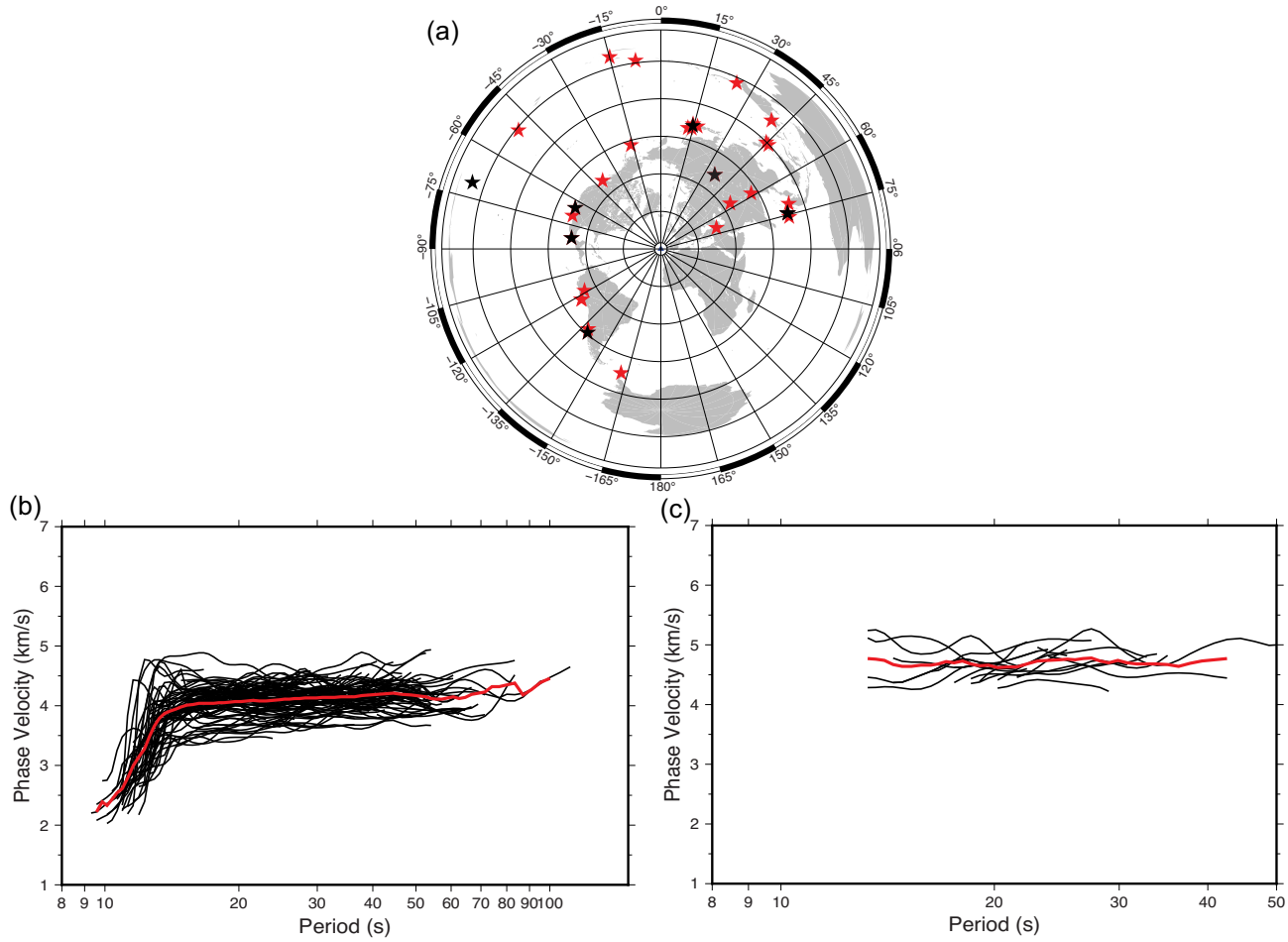

Figure 3. (a) Teleseismic earthquakes used in the two-station method for the hydrophone (red and black stars) and transverse components (black stars only). (b) Phase velocity dispersion curves extracted from the hydrophone with the two-station method for 32 events (black lines) and average of all dispersion curves (red line). (c) Same as (b), but for the transverse component and using only eight teleseismic events due to the lower SNR.

5 km thickness until the model's maximum depth of 200 km. These layer thicknesses were fixed during the inversion. We tested starting models with a water velocity of $Vp = 1.5\,\mathrm{km\,s^{-1}}$ and $Vs = 0\,\mathrm{km\,s^{-1}}$, a sedimentary layer varying between $Vp = 2.23$–$3.27\,\mathrm{km\,s^{-1}}$ and $Vs = 0.75$–$1.65\,\mathrm{km\,s^{-1}}$, and a half-space velocity varying between $Vp = 6.32$–$8.2\,\mathrm{km\,s^{-1}}$ and $Vs = 3.65$–$4.55\,\mathrm{km\,s^{-1}}$ (Fig. S2, Supporting Information). The range of velocities for the sediments was set considering the significant variability observed from consolidated ($Vs = 1.65\,\mathrm{km\,s^{-1}}$) to unconsolidated sediments ($Vs = 0.75\,\mathrm{km\,s^{-1}}$, Shillington *et al.* 2008; Zimmer *et al.* 2002). Additionally, we also considered local models for the study area, which show that the *S*-wave velocities of sediments range from 1 to $1.9\,\mathrm{km\,s^{-1}}$ (Batista *et al.* 2017) and from 0.7 to $1.4\,\mathrm{km\,s^{-1}}$ (Hannemann *et al.* 2016).

In the first 2 iterations of the inversion, we set the damping to a high value of 10 to avoid overshooting in the first model estimation. After the second iteration, the damping was decreased to 1 for the rest of the 20 iterations. Fig. S2 (Supporting Information) shows that regardless of the starting model the final *Vs* models are very stable over all depths, except when the velocities are very low in the initial model. Thus, we decided to use for our starting model $Vs = 1.3\,\mathrm{km\,s^{-1}}$ for the sediments, in agreement with the local models previously obtained by Batista *et al.* (2017) and Hannemann *et al.* (2016), and $Vs = 4.0\,\mathrm{km\,s^{-1}}$ for the half-space.

To quantify the depth sensitivity of group and phase velocities of Love and Rayleigh waves, we calculated the respective sensitivity kernels using our final *Vs* model (see Fig. S3, Supporting Information). Different wave periods are sensitive to different depths, with the longer periods observed in our study ($T \sim 40$ s) allowing to sample the structure until a depth of 80 km. The sensitivity kernels confirm a reduced sensitivity of Rayleigh waves to the crustal structure due to the water layer.

4.2 3-D surface wave tomography

The 3-D surface wave tomography is done in two steps. In the first step, we performed a 2-D inversion to obtain, for each period, laterally varying Love wave group velocity maps. In the second step, we inverted the 2-D Love wave group velocity maps, further constrained by the average Love and Rayleigh wave phase velocities for the region, to obtain a 3-D *S*-wave velocity model.

In order to obtain 2-D group velocity maps for the various observation periods, we used the fast marching surface tomography (FMST) method of Rawlinson (2005). This method provides stable and robust solutions in complex laterally heterogeneous media. For the inversion of the 2-D velocity maps, we used only the group velocity of Love waves, because of the reduced number of paths observed in the phase velocity of Love waves.

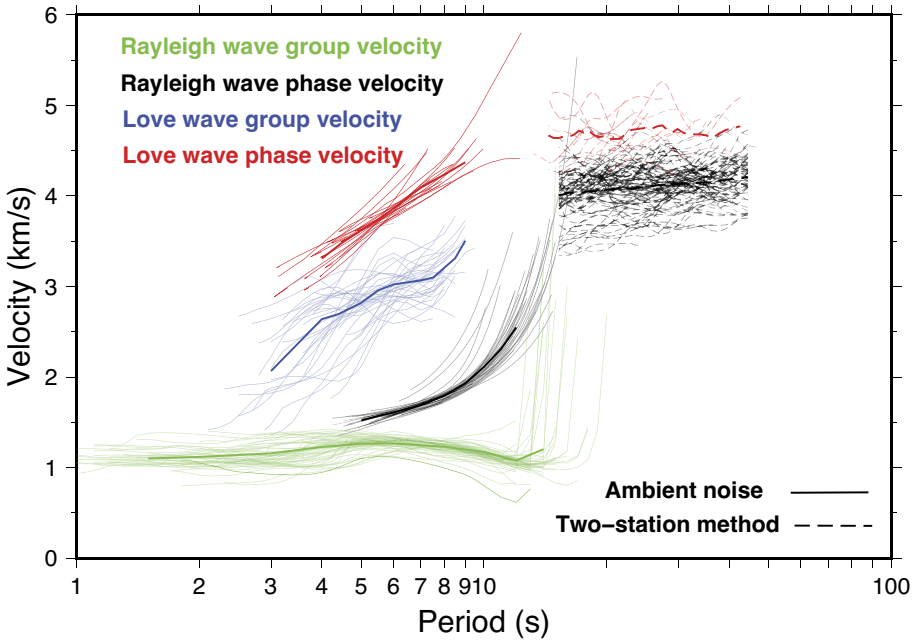

Figure 4. All dispersion curves measured for Love waves (transverse component, blue and red) and Rayleigh waves (hydrophone, green and black). Phase velocities are shown in black or red, and group velocities are shown in green or blue. Short-period observations (< 14 s) were obtained from ambient seismic noise (solid lines) and long-period observations (> 14 s) from the two-station analysis (dashed lines). Thick lines are the averages of the observed dispersion curves obtained for all paths.

Table 1. Table of data used for the 1-D shear velocity inversion.

Method	Wave	Period (s)
Ambient noise	Love wave group velocity	3–9
Ambient noise	Love wave phase velocity	4–9
Two station	Love wave phase velocity	14–42
Two station	Rayleigh wave phase velocity	15–44

To quickly estimate the lateral resolution of the Love wave group velocity maps, we tested 2-D checkerboards parametrized using block sizes of $0.2^\circ \times 0.2^\circ$ and $0.26^\circ \times 0.26^\circ$ for periods of 4, 6 and 7 s. For each period, the starting velocity corresponds to the average velocity of the various observations. Fig. S4 (Supporting Information) shows the recovery of the checkerboard with a perturbation of $\pm$ 0.8 per cent and picking errors of 0.1 s. Cells of $0.2^\circ \times 0.2^\circ$ show a much better recovery of the synthetic anomalies. The checkerboard tests show that we can recover features with a scale of approximately 23 km.

We tested different values of the smoothing (η) and damping (ε) regularization parameters used to stabilize the inversion (Rawlinson *et al.* 2006) (see Text S1, Supporting Information). The analysis of the L-shaped trade-off curves (Fig. S5, Supporting Information) revealed that a smoothing $\eta = 20$ and damping $\epsilon = 10$ are the best compromises for the inversion.

Love wave group velocity data from 4 to 8.5 s were inverted using the previously defined smoothing and damping parameters. This period band was chosen based on the number of interstation paths. Fig. S6 (Supporting Information) shows the 2-D Love wave group velocity maps together with the bathymetry contour.

To build the final 3-D shear wave velocity model, we inverted the Love wave group velocities for each point of the grid of $0.2^\circ \times 0.2^\circ$. At each node, we complemented the laterally varying Love wave group velocity maps with the average of Love wave phase velocities between 4 and 9 s measured from seismic ambient noise and the average of teleseismic surface wave Love wave and Rayleigh wave phase velocities between 14 and 42 s and 15 and 44 s, respectively, measured from the two-station method (Table 1).

The horizontal resolution of the 3-D shear wave velocity model is similar to the one inferred from the checkerboards tests of the 2-D group and phase velocity maps. The vertical resolution of 3-D shear wave velocity models obtained from surface wave tomography depends on the period range considered. These periods limit the maximum depth that we can interpret. We use the sensitivity kernels to infer the depth sensitivity and examine the resolution matrix per grid node obtained from the surface wave inversion. The sensitivity kernels show that we can safely interpret our model until a depth of 10 km. In addition, the resolution matrix indicates that the best resolution is attained between 2 and 6 km depth (Fig. S7, Supporting Information).

5 RESULTS

Our final 1-D shear wave velocity model is shown in Fig. 5, as well as the fit between measurements and model predictions. The root mean square obtained for the 1-D inversion is 0.0062 km s^{-1} for the last iteration, indicating a good data fit. Note that no radial anisotropy was necessary to simultaneously fit Love and Rayleigh waves dispersion curves.

The final 1-D model shows the fixed water layer of 5 km, below which we find a sediment layer with a $Vs = 1.05$ km s^{-1}, lower than the initial model. The sediments are followed by a rapid increase to crustal velocities, which rise from 3.4 km s^{-1} at 5.6 km to 4.9 km s^{-1} at 15.6 km depth. Between 16 and 36 km, below the crust, we observe a fast velocity zone of ~4.9 km s^{-1} and ~20 km thickness. This fast velocity zone is followed by a decrease in *S*-wave velocities, reaching a minimum of 4.6 km s^{-1} at approximately 70 km depth.

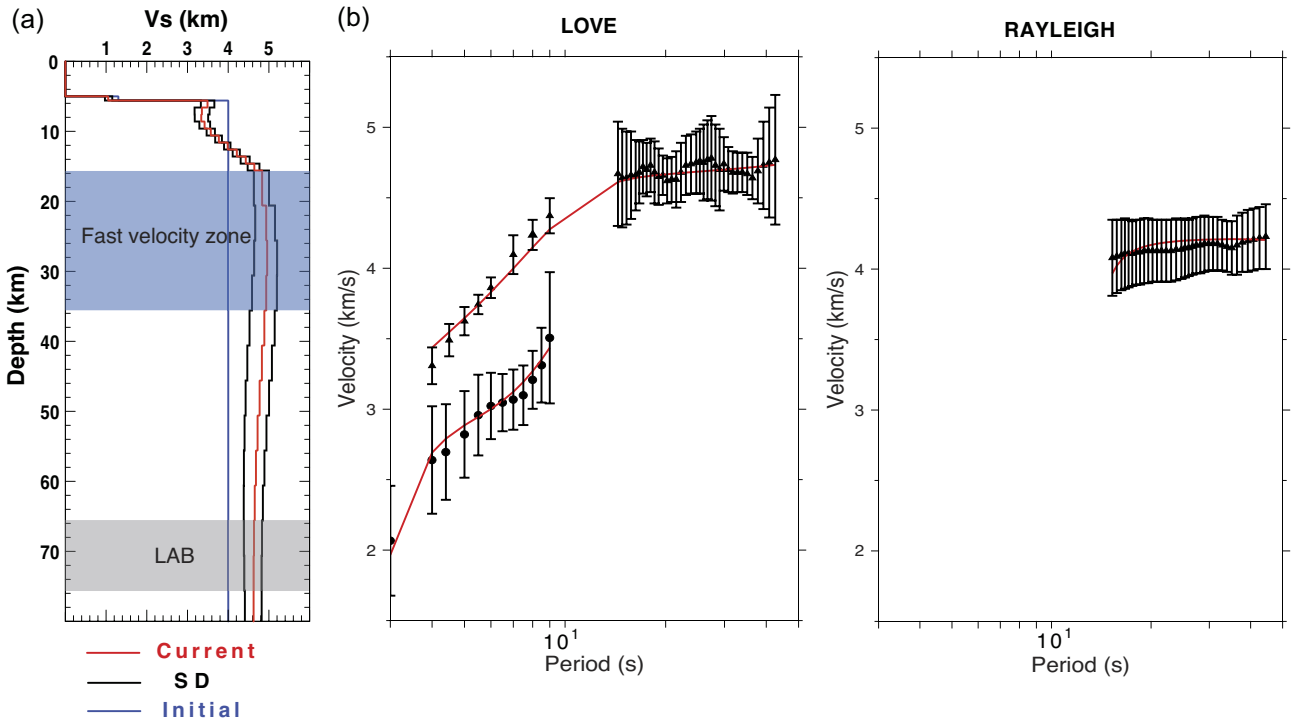

Figure 5. Final 1-D shear wave velocity model for the DOCTAR area based on the surface wave dispersion inferred from ambient noise and the two-station methods. (a) Final 1-D shear wave model (solid red line), minimum and maximum error bars of the single standard deviation of the dispersion curves by each period (solid black line) and the initial half-space model (solid blue line) down to a depth of 80 km. (b) Observed average Rayleigh and Love waves dispersion curves (triangles represent the phase velocity and circles the group velocity measurements) and dispersion curve corresponding to the best-fitting model after 20 iterations (red line).

The 3-D tomographic model of the region is shown in Fig. 6, in *Vs* horizontal slices at different depths ranging from 2 to 10 km below the seafloor. Velocity anomalies are shown in percentage with respect to the average shear wave velocity at each depth, which is shown at the top-right of each depth plot. At a depth of 2 km, a fast-velocity anomaly that is ∼5 per cent faster than the average velocity is observed to the northwest of the array and a low-velocity anomaly of ∼ 3 per cent is seen in its central region. The strongest low-velocity anomaly starts to appear at 4 km depth to the southwest. A weaker low-velocity anomaly is found to the northwest, which is best observed at 5 km depth. These two low-velocity anomalies, with amplitudes of ∼5 per cent and ∼4 per cent with respect to the average velocities, extend down to 9 km depth. In addition, fast-velocity features become visible at 4 km depth below the ocean floor to the north, south, centre and east of the array, located below small mountains. These fast-velocity anomalies are on average ∼3.5 per cent faster than the average velocity at this depth, and extend to a depth of 8 km, with the fast-velocity anomaly in the centre of the array extending down to a depth of 10 km. At 9 and 10 km depth, the velocity anomalies start to become smeared as resolution starts to decrease.

The lateral anomalies are better understood in vertical cross-sections through the 3-D model. Fig. 7 presents several vertical profiles that extend from 1 to 15 km depth, together with the corresponding seafloor bathymetry (note the vertical exaggeration). Whereas Fig. 6 showed relative anomalies, Fig. 7 shows absolute *S*-wave velocities. To better characterize the changes in velocity, we plotted isocontours each 0.5 km s^{-1}. For reference, we plot a Moho boundary at 7 km depth as a grey dashed line, after Crust 1.0 (Laske *et al.* 2013). In addition, we also mark with crosses the Moho depths below each OBS inferred by Hannemann *et al.* (2016) using receiver functions. Two profiles, P3–D07 and D09–D11, are perpendicular to the GF; profiles P1–P1′, D10–D12 and P2–P2′ are parallel to the GF; and the last profile, D08–D06, is oblique and oriented southwest-northeast. Although for visualization purposes we plotted the profiles until 15 km, we should keep in mind that the lateral resolution is only good until 10 km depth. The dominant image revealed by the tomographic cross-sections is that of a layered structure with lateral oscillations, whose amplitudes decrease with depth.

In detail, at shallow depths we observe in all profiles a strong variation of the 3.5 km s^{-1} velocity isocontour (Fig. 7). Between stations D09 and D01 (profile D09–D11), we observe the shallowest 3.5 km s^{-1} isocontour of the entire study area, consistent with the presence of a fast-velocity anomaly between 4 and 8 km (Fig. 6). The deepest 3.5 km s^{-1} isocontour is observed between stations D08 and D03 (profile D08–D06) and is related to a strong low-velocity anomaly observed in the *Vs* maps. Profiles P3–D07 and D10–D12 show a more homogeneous *S*-wave velocity structure. The velocity isocontour of 4 km s^{-1} shows a maximum depth of 7.5 km to the northwest and southwest of the study area, which is clearly observed in profiles D08–D06, P1–P1′ and P2–P2′. A minimum depth of ∼6 km for this isocontour is found to the south and centre of the DOCTAR area.

6 DISCUSSION

6.1 Local vertical structure (1-D model)

In order to better interpret our results, we plotted our final 1-D model together with those of previous studies for the same study region (Hannemann *et al.* 2016; Batista *et al.* 2017), a more general

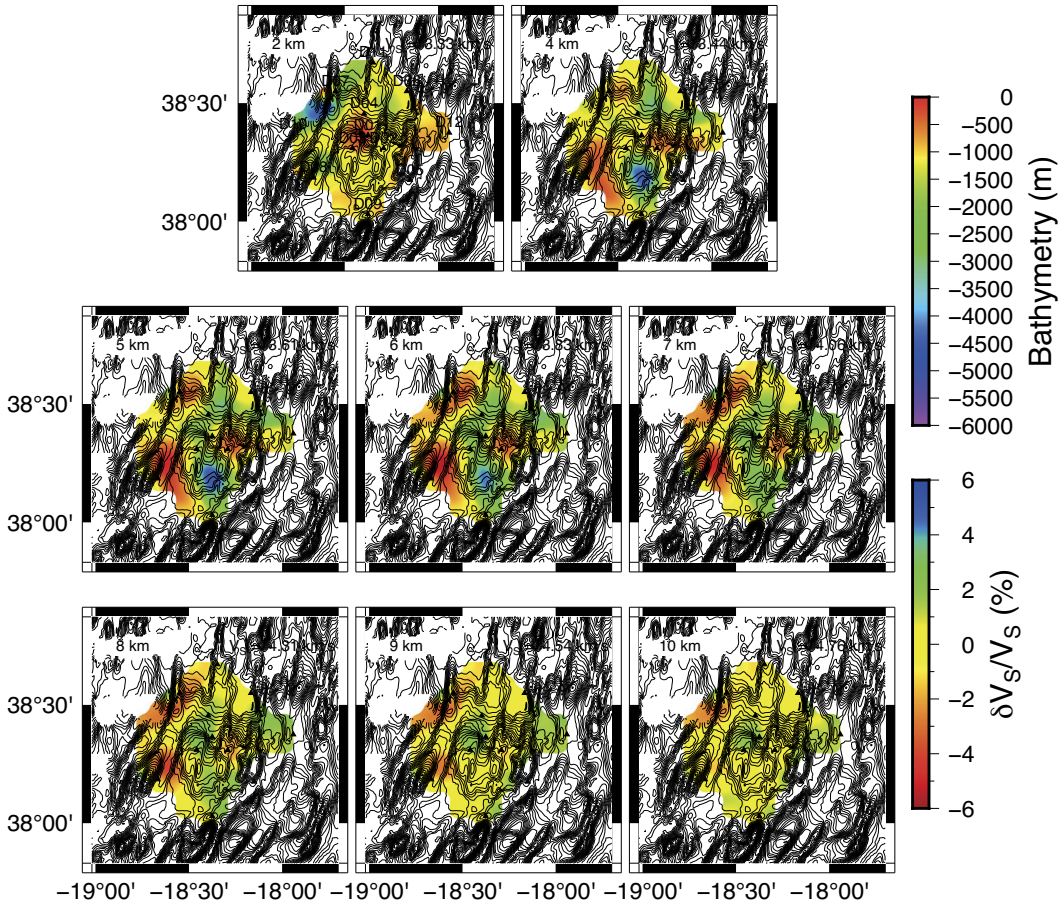

Figure 6. Horizontal slices through the 3-D shear wave tomographic model at depths from 1 km down to 10 km below the sea level. The topography is shown in the background as contours.

model of the oceanic crust after White *et al.* (1992), and one deeper model of oceanic lithosphere of similar age (70 Ma Pacific Ocean) by Lin *et al.* (2016, Fig. S8, Supporting Information).

Our 1-D model shows a sediment layer with a velocity of $Vs = 1.05\,\mathrm{km\,s^{-1}}$, a value that is low but within the ranges inferred by previous studies in the region (Hannemann *et al.* 2016; Baptista *et al.* 2017). We interpret this low value as indicating the presence of clay sediment pockets associated with the rough bathymetry (NOAA World Data Service for Geophysics, Marine Seismic Reflection, Survey ID V2707, ngdc.noaa.gov).

Surface waves are not sensitive to discontinuities; therefore, we cannot infer the exact depth of the Moho. However, we can estimate the crustal thickness assuming a value for the velocity at the top of the mantle. If we consider reference models, such as the Oceanic Parametric Earth Model or Crust1.0 (Dziewonski *et al.* 1975; Laske *et al.* 2013), the upper-mantle shear wave velocity below the Moho should be $4.5\,\mathrm{km\,s^{-1}}$. In this case, we would find our total crustal thickness to be 9 km. However, if instead we use a topmost mantle of $Vs = 3.9\,\mathrm{km\,s^{-1}}$, as found by Batista *et al.* (2017) for the base of layer 4 (L4), then we infer a crustal thickness of 6 km. Our model thus loosely constrains the crustal thickness to be in the range between 6 and 9 km, that is, tendentially thicker than the usually reported for the slow-spreading Atlantic ridge at various latitudes, away from the influence of hotspots (e.g. Wang *et al.* 2011; Vaddineni *et al.* 2021; Wang & Singh 2022). In spite of suggestions that the proximity to a major oceanic transform fault will cause mantle serpentinization (White *et al.* 1992), we find no clear indication of serpentinization, as would be indicated by lower *Vs* and higher Poisson´s ratio (e.g. Kamiya & Kobayashi 2000).

The 1-D vertical profile depicts a near-constant velocity layer between 16 and 35 km depth that shows a very high $Vs \approx 4.9\,\mathrm{km\,s^{-1}}$, namely in comparison to the model of oceanic lithosphere of Lin *et al.* (2016, Fig. S8, Supporting Information). At these uppermost mantle depths, the dominant peridotite rocks have lherzolite compositions that are characterized by the presence of olivine, orthopyroxene, clinopyroxene and plagioclase (e.g. Wang *et al.* 2013). The low *Vs* that characterizes plagioclase ($3.54\,\mathrm{km\,s^{-1}}$) and clinopyroxene ($4.66\,\mathrm{km\,s^{-1}}$, Wang *et al.* 2013) suggests that the dominant minerals in our study region at those depths are olivine ($4.82\,\mathrm{km\,s^{-1}}$) and orthopyroxene ($4.86\,\mathrm{km\,s^{-1}}$), forming harzburgites.

In oceanic settings, harzburgites and dunites are found in subduction zones or island arc collisions, but also in mid-ocean ridges (Kelemen *et al.* 1995; Rospabé *et al.* 2021). Phase equilibrium modelling, for mantle anhydrous peridotite melting that generates Mid-Ocean Ridge Basalt (MORB), was recently performed by Gardiner *et al.* (2019) using the most updated thermodynamic internally consistent data set and activity-composition solution models. Their study supports the long-standing results of experimental petrology (e.g. Barker & Stolper 1994) on the role of clinopyroxene consuming reactions during melting, leading to the exhaustion of this mineral on the melting residue, for melt fraction around 15 per cent volume. Thus, partial melting of a lherzolite can originate a residual harzburgite if the extent of partial melting is substantial ($\geq$ 15 per cent). The spreading at the Mid-Atlantic Ridge is slow when

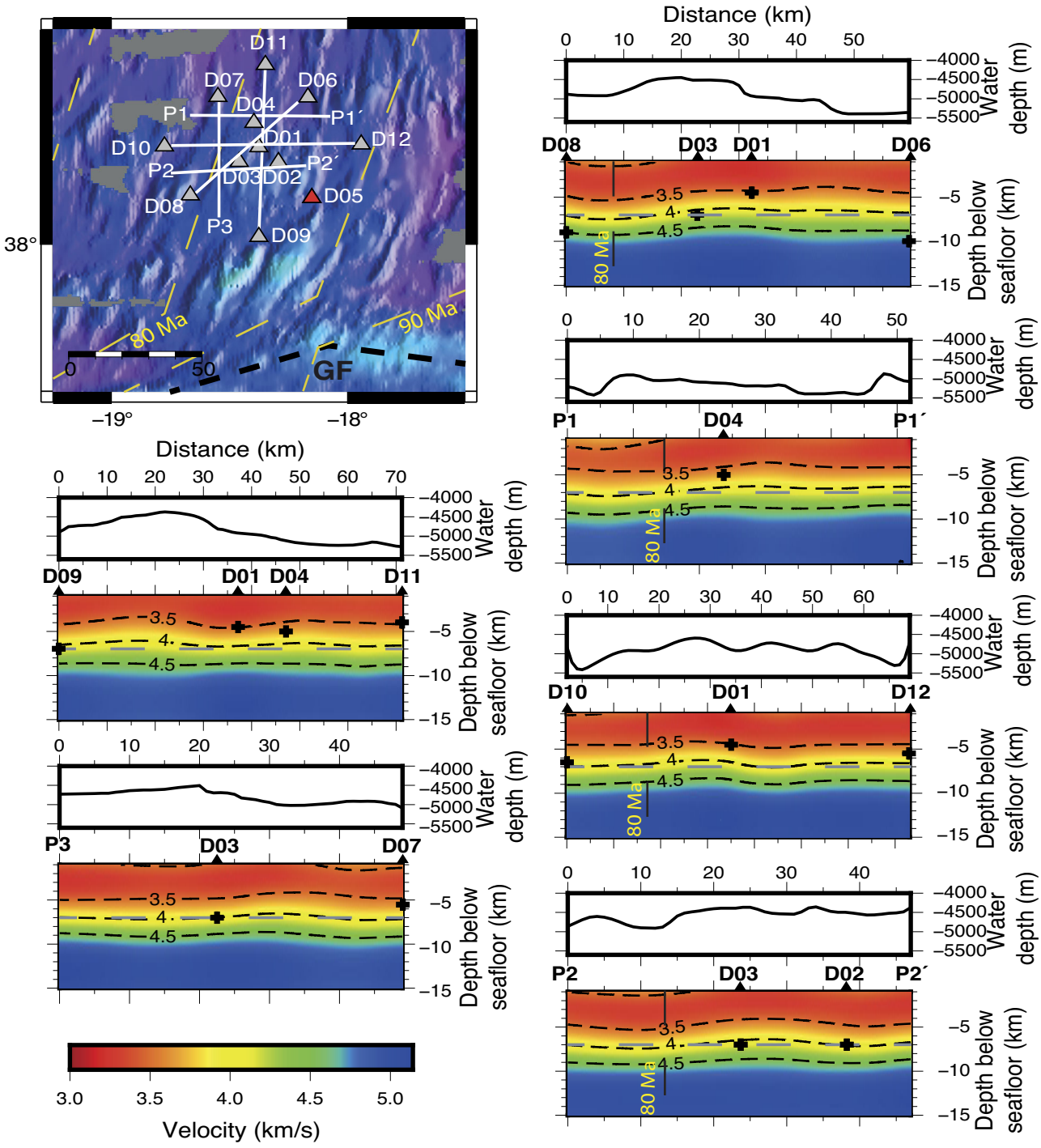

Figure 7. Selected vertical cross-sections through the 3-D shear wave tomographic model. The map on the top-left depicts the study area, showing OBS stations (grey triangles) and the selected profiles (white lines). The background shows the bathymetry (www.gebco.net) and yellow lines show the ages of the oceanic crust (Müller *et al.* 2008). Along the cross-sections, we plot *Vs* contours with increments of 0.5 km s^{-1}. The grey dashed line marks the Moho according to Crust1.0 (Laske *et al.* 2013) and the back crosses mark the Moho inferred from receiver functions below the OBS by Hannemann *et al.* (2017).

compared with the Pacific (e.g. Müller *et al.* 2008), which would imply relatively low percentage of partial melting during the generation of MORB (e.g. White et. al. 2001). Indeed, according to these authors the fraction of melting decreases significantly with the decreasing of spreading rate, with values of < 15 per cent vol. found for ridges with rates of spreading ≤ 20 mm yr^{-1}. However, the amount of melting at a ridge is also influenced by the presence of mantle anomalies such as hotspots, as was initially proposed by Dick *et al.* (1984) and Niu & Hékinian (1997). Both geochemical (e.g. Madureira *et al.* 2005; Beier *et al.* 2010) and seismic tomographic (e.g. Silveira *et al.* 2006; Yang *et al.* 2006; Beier *et al.* 2022) studies have associated the Azores Plateau and islands with the presence of a mantle plume, which also explains the estimated Azores mantle potential temperature, some 120 °C in excess of

those that typically characterize the generation of normal MORB (N-MORB, Putirka 2008). Geochemical and bathymetric gradients along the ridge near the Azores Plateau have been considered as evidence of plume–ridge interaction (e.g. Dosso *et al.* 1999; Moreira & Allègre 2002; Dalton *et al.* 2014; Madureira *et al.* 2014). This implies the influence of plume heat and mass on the genesis of MORB in the area. Consequently, the generation of MORB along ridge segments in the vicinity of the Azores Plateau happened at potential temperatures clearly above those typical of N-MORB (see Dalton *et al.* 2014).

The present location of the Azores hotspot is usually placed under the Azores Plateau, close to the central group of islands as depicted by studies of tomography (Yang *et al.* 2006) and noble gases (Moreira *et al.* 2018). The generation of the plateau started at about 20 Ma (Gente *et al.* 2003; Luís & Miranda 2008), that is, in times significantly more recent than the formation of the ocean crust of the DOCTAR area (≈80 Ma according to Müller *et al.* 2008). However, we emphasize that the Azores plume should have impinged the lithosphere by 85 Ma (e.g. Gente *et al.* 2003; Ribeiro *et al.* 2017) and that the hotspot–ridge interaction may have been active since then (Gente *et al.* 2003). In this scenario, the fraction of melt would have been clearly higher than 15 per cent, according to the pseudo-section calculated by Gardiner *et al.* (2019), resulting in a harzburgite (olivine + orthopyroxene) residue.

Thus, we propose that the high *Vs* detected in the study region reflects the presence of harzburgite, a refractory residue of enhanced melting due to the proximity between the Azores mantle plume in its earlier stages and the Mid-Atlantic Ridge. The hypothetical presence of dunitic veins, usually interpreted by melt/harzburgite reaction (e.g. Kelemen *et al.* 1995), would not significantly alter the shear wave velocities and our interpretation. In their study of local seismicity, Krüger *et al.* (2020) found shallow hypocenter earthquakes in the GF domain extending down to 30 km depth, which is approximately the depth at which *Vs* starts to decrease below the inferred harzburgite high-velocity layer. Thus, earthquake generation seems to be confined to the topmost, faster materials above 30 km depth.

Using receiver functions, Hannemann *et al.* (2017) imaged the LAB below the DOCTAR area at ∼70–80 km depth. Because surface waves are not sensitive to the exact location of interfaces, the inference of the LAB from models based on these data is not straightforward. Previous studies have taken as a proxy for the depth of the LAB the minimum *Vs* or the *Vs* maximum negative gradient (steepest decrease in *Vs*), among others (Burgos *et al.* 2014; Rychert *et al.* 2020). In our model, the minimum *Vs* is imaged at a depth of ∼70 km. The steepest decrease in *Vs* occurs above 70 km. However, given the presence of the fast-velocity layer at 16–36 km and the smoothness of the model below this layer, the maximum gradient is observed at the bottom of the fast velocity layer with a gradual decrease downwards. Thus, we cannot estimate the LAB depth from the maximum gradient criterion; we can only conclude that the LAB is located at a maximum depth of 70 km, consistent with the results of Hannemann *et al.* (2017).

The oceanic LAB is usually considered to reflect the half-space cooling of the lithosphere (e.g. Niu & Humphrys 2009). If we consider that in the study area, the mean age of ocean crust is about 80 Ma (Müller *et al.* 2008) and the age versus thickness equation used by Niu & Humphrys (2009), the LAB should occur at ≈ 90 km depth. The LAB can be thought of as a rheological contrast between the outermost cold rocks not readily deformed over geologic time (lithosphere and rigid behaviour) and the underlying deformable asthenosphere (ductile behaviour at mantle potential temperature conditions). Therefore, the LAB can generally be taken as corresponding to an isotherm (e.g. Turcotte & Schubert 2014).

The significant difference between the LAB depth estimated from our *Vs* 1-D model and the predictive depth from the half-space cooling model suggests that in our study region the LAB depth does not result from the usual cooling trend of oceanic lithosphere. The shallower than expected LAB depth suggests that the interaction between the mid-ocean ridge and the Azores plume is still reflected today in the lithospheric structure of the DOCTAR area.

In alternative or concurrently, we should also keep in mind that the dextral-transcurrent motion of the GF generates heat flow due to friction between the Nubia and the Eurasian plates. Higher heat flow can be found up to 60 km away from the fault in the vicinity of the San Andreas Fault, California, which is also a transform fault (Scholz 2002). The closest DOCTAR station to the GF (D09) is located at a distance of ∼40 km from the fault. Thus, the additional frictional heat from the GF could cause the LAB to be shallower than expected in our study region.

6.2 Tomographic laterally varying structure (3-D model)

The 3-D tomographic model shown in Figs 6 and 7 reveals a layered seismic structure from 2 km to the deepest inverted depth, recognizing a relatively homogeneous crust and uppermost mantle. The strongest high- and low-velocity anomalies, with amplitudes of about ± 5 per cent, are more prominent between 4 and 8 km. In almost all cross sections (Fig. 7), we image oscillations of the crustal structure, which are clearly visible in the isocontours. The amplitudes of these oscillations are in the order of 1 km in the 4 km s^{-1} isocontour and 0.5 km for the 4.5 km s^{-1} isocontour.

An important question is whether these oscillations are well resolved. An approximation that we made in our modelling concerned the water layer thickness, which is variable across the array but which we approximated as a layer with a constant thickness of 5 km. Ocean floor relief changes across the DOCTAR array are smooth in comparison with topographic differences between abyssal plains and continental shelves. In a previous study, Ko¨hler *et al.* (2012) demonstrated that the effect of the topography on phase velocity dispersion measurements is only relevant for periods ≤ 5 s when strong topography changes are considered, further adding that the maximum effect for any mountain range on Earth does not exceed ∼ 0.7 per cent globally.

A visual inspection of bathymetric profiles along selected cross-sections through our 3-D model does not show an obvious relationship between seafloor bathymetry and the imaged oscillations of the crustal structure (Fig. 7). In addition, the oscillations show a wavelength of about 25–30 km and therefore lay within the resolution of our model. Crustal structure oscillations are also seen in the previous nearby studies of Batista *et al.* (2017) and Hannemann *et al.* (2016). The oscillations are more evident in the W-E profile of Hannemann *et al.* (2016) and in layer L3 in the model of Batista *et al.* (2017). The oscillations therefore appear to be robust, although their short-scale characteristics cannot be resolved by our 3-D model.

Given the correlation usually accepted between magma supply rate at ridges and ocean crustal thickness (e.g. Zhou *et al.* 2020; Liu *et al.* 2022), we interpret the crustal oscillations as reflecting a non-steady-state behaviour of magmatic processes at the slow-spreading Mid-Atlantic Ridge. Previous studies have shown oscillations of crustal thickness in profiles perpendicular to the Mid-Atlantic Ridge (e.g. Pariso *et al.* 1995; Tucholke *et al.* 1997; Bonatti *et al.* 2003; Shinevar *et al.* 2019). The DOCTAR area is located in

oceanic crust with ages between 75 and 85 Ma, with an age difference of 10 Ma from station D10 to D12. In our 3-D model, we image crustal oscillations with wavelengths of ∼25–30 km, which is in good agreement with the values previously reported for this slow-spreading ridge, whose evolution seems to be controlled by punctuated magma pulses.

7 CONCLUSIONS

We computed both a vertical 1-D and a full 3-D shear wave velocity model for the DOCTAR area (eastern mid-Atlantic Ocean; ∼70 km north of the GF). Both models were obtained from the analysis of surface waves recorded on OBS, using ambient seismic noise and teleseismic surface aves. The 1-D model shows an oceanic crust with a low-velocity sediment layer of 1.05 km s^{-1}, associated with clay sediments. Below the sediments, we find an oceanic crust with velocities ranging from 3.3 to 4.5 km s^{-1}. In addition, we find a 20 km layer below the crust, between 16 and 36 km depth, with very fast velocities of ∼4.9 km s^{-1}, which we attribute to the presence of harzburgite, a refractory residue of enhanced melting generated by the proximity between the Mid-Atlantic Ridge and the Azores mantle plume. The velocity decreases below this fast layer, reaching a minimum of 4.6 km s^{-1} at ∼70 km depth, which we interpret as the LAB. This depth inferred for the LAB is in good agreement with that reported by Hannemann *et al.* (2017) for the same region. However, the inferred LAB depth is shallower than would be expected from a simple cooling model of oceanic lithosphere for the age of our study region (90 km). Our shallow LAB suggests the presence of an additional heat source, which we hypothesize that can be the nearby Azores plume and/or the friction heat generated by the nearby GF.

Our 3-D *Vs* model images a dominantly layered structure, with lateral crustal oscillations with wavelengths of ∼25–30 km. Hannemann *et al.* (2016) also observed such oscillations in the 2-D model, especially in their W-E profile. These oscillations may be related to changes in the rates of mantle upwelling during the formation of the crust. In addition, the dextral-transcurrent motion of the GF may have additionally deformed the lithosphere, as observed in the shearing of the topography.

Our 1-D vertical and the 3-D tomographic models for the crust and uppermost mantle contribute to constraining the structure and processes at the slow-spreading Atlantic, in this particular area characterized by plume–ridge interaction and close to a major oceanic strike-slip fault.

ACKNOWLEDGMENTS

Especial thanks to DEPAS pool (Deutsche Geräte-Pool für Amphibische Seismologie) for providing the instruments for the DOCTAR project, which was funded by the DFG (KR1935/13 and DA 478/21-1) and by the Leitstelle für Mittelgroße Forschungsschiffe (Poseidon cruises 416 and 431). Figures were generated with the Generic Mapping Tools software (GMT 5, Wessel *et al.* 2013). Data pre-processing was done using SAC—Seismic Analysis code (Goldstein & Snoke 2005). This work was funded by the Portuguese Fundação para a Ciência e a Tecnologia (FCT) I.P./MCTES through national funds (PIDDAC)—UIDB/50019/2020 and the FCT fellowship PD/BD/135069/2017.

DATA AVAILABILITY

DOCTAR data are available upon request.

SUPPORTING INFORMATION

Supplementary data are available at *GJI* online.

Figure S1. Example of Rayleigh wave phase velocity measurement for the station D01H–D06H with an interstation distance of 27.42 km. (a) Waveform of the same teleseismic earthquake recorded at stations D01 and D06. (b) Cross-correlations between the waveforms recorded at the two stations and their respective time–frequency representation. (c) 2π ambiguous measured phase velocity dispersion curve (blue lines) plotted together with the reference model (thick grey dashed line) and the normalized amplitude spectrum of the cross-correlation function (black dashed line). (d) Selected phase velocity dispersion curves for these two pair of stations (red curve).

Figure S2. (a) Shear wave velocity models were obtained using different starting models. For the different starting models, the velocity of the sediments and the half-space were varied by ± 0.5 km s^{-1}. (b) The final shear velocity models are very stable over all the depths where each colour represents a different initial model. The strong red on the right edge is the chosen initial velocity model and has a half-space velocity of 4 km s^{-1}. (c) Fit to the dispersion data of each tested model (green) and the selected initial model (red).

Figure S3. Sensitivity kernels computed as group and phase velocity derivatives with respect to the shear velocities at 4 and 9 s (top panels) and 20, 30, 42 and 44 s periods (bottom panels). All layers of the final 1-D model were divided into 1 km layers.

Figure S4. Checkerboard resolution test for the group velocity of Love waves. (a) Input model with dimensions of 0.26° × 0.26° for 4, 6 and 7 s period and a velocity perturbation of 0.8 per cent. The recovery of the inversions is shown in the right where the reference velocity is taken by averaging the velocity observations of each period using the available paths. (b) Checkerboard for blocks size of 0.2° × 0.2°.

Figure S5. Trade-off curves between data variance and model roughness used to estimate the optimal damping and smoothing parameters. The damping factor prevents the solution model from straying too far from the initial model, while the smoothing factor constrains the smoothness of the solution model. (a) Variation of the smoothing parameter for a fixed damping parameter with $\epsilon = 1$ for the 2-D inversion of group velocities of Love waves at 6 s period. The value of $\eta = 20$ is chosen as preferred. (b) Variation of the damping parameter fixing the smoothing at $\eta = 20$. $\epsilon = 10$ were chosen as the optimum value. (c) Evolution of data variance with iteration using the damping and smoothing parameters selected in (a) and (b). The inversion converges after four iterations.

Figure S6. 2-D Love wave group velocity maps at increasing periods from 4 to 8.5 s. We used the FMST method to compute the group velocity maps. The figure is plotted as relative velocity with respect to the average of the velocity map.

Figure S7. Vertical resolution of the 3-D shear wave velocity model, in terms of the resolution matrix diagonal element (RDE) values. The best resolution is obtained until 6 km depth.

Figure S8. Comparison of the 1-D final shear wave velocity model obtained in this work (black line) with other regional models, namely Hannemann *et al.* (2016, red line) and Batista *et al.* (2017, green line), one deep profile of 70 Ma Pacific lithosphere by Lin *et al.* (2016, purple line) and a general oceanic model from White *et al.* (1992, blue line).

Oxford University Press is not responsible for the content or functionality of any supporting materials supplied by the authors.

Any queries (other than missing material) should be directed to the corresponding author for the paper.

REFERENCES

Baker, M.B. & Stolper, E.M. 1994. Determining the composition of high-pressure mantle melts using diamond aggregates. *Geochim. Cosmochim. Acta,* **58**(13), 2811–2827.

Batista, L., Hübscher, C., Terrinha, P., Matias, L., Afilhado, A. & Lüdmann, T. 2017. Crustal structure of the Eurasia–Africa plate boundary across the Gloria Fault, North Atlantic Ocean. *Geophys. J. Int.,* **209**(2), 713–729.

Beier, C., Genske, F., Hübscher, C., Haase, K.M., Bach, W. & Nomikou, P. 2022. The submarine Azores Plateau: evidence for a waning mantle plume? *Mar. Geol.,* **451,** 106858, https://doi.org/10.1016/j.margeo.2022.106858.

Beier, C., Turner, S., Plank, T. & White, W. 2010. A preliminary assessment of the symmetry of source composition and melting dynamics across the Azores plume. *Geochem. Geophys. Geosystems.,* **11**(2), 1–14.

Bensen, G.D., Ritzwoller, M.H., Barmin, M.P., Levshin, A.L., Lin, F., Moschetti, M.P., Shapiro, N.M. & Yang, Y. 2007. Processing seismic ambient noise data to obtain reliable broad-band surface wave dispersion measurements. *Geophys. J. Int.,* **169**(3), 1239–1260.

Bonadio, R. *et al.* 2018. Hot upper mantle beneath the Tristan da Cunha hotspot from probabilistic rayleigh-wave inversion and petrological modeling. *Geochem. Geophys. Geosyst.,* **19**(5), 1412–1428.

Bonatti, E., Ligi, M., Brunelli, D., Cipriani, A., Fabretti, P., Ferrante, V., Gasperini, L. & Ottolini, L. 2003. Mantle thermal pulses below the Mid-Atlantic Ridge and temporal variations in the formation of oceanic lithosphere. *Nature,* **423**(6939), 499–505.

Buforn, E., Udías, A. & Colombás, M. 1988. Seismicity, source mechanisms and tectonics of the Azores-Gibraltar plate boundary. *Tectonophysics,* **152**(1-2), 89–118.

Burgos, G., Montagner, J.-P., Beucler, E., Capdeville, Y., Mocquet, A. & Drilleau, M. 2014. Oceanic lithosphere/asthenosphere boundary from surface wave dispersion data. *J. geophys. Res. Solid Earth,* **119,** 1079–1093.

Carvalho, J., Bonadio, R., Silveira, G., Lebedev, S., Mata, J., Arroucau, P., Meier, T. & Celli, N.L. 2019. Evidence for high temperature in the upper mantle beneath Cape Verde archipelago from Rayleigh-wave phase-velocity measurements. *Tectonophysics,* **770**(October), doi:10.1016/j.tecto.2019.228225

Carvalho, J., Silveira, G., Kiselev, S., Custódio, S., Ramalho, R.S., Stutzmann, E. & Schimmel, M. 2022. Crustal and uppermost mantle structure of Cape Verde from ambient noise tomography. *Geophys. J. Int.,* **231**(2), 1421–1433.

Dalton, C.A., Langmuir, C.H. & Gale, A. 2014. Geophysical and geochemical evidence for deep temperature variations beneath mid-ocean ridges. *Science,* **344**(6179), 80–83.

DeMets, C., Gordon, R.G. & Argus, D.F. 2010. Geologically current plate motions. *Geophys. J. Int.,* **181**(1), 1–80.

Dick, H., Natland, J. & Ildefonse, B. 2006. Past and future impact of deep drilling in the oceanic crust and mantle. *Oceanography,* **19**(4), 72–80.

Dick, H.J., Fisher, R.L. & Bryan, W.B. 1984. Mineralogic variability of the uppermost mantle along mid-ocean ridges. *Earth planet. Sci. Lett.,* **69**(1), 88–106.

Dosso, L., Bougault, H., Langmuir, C., Bollinger, C., Bonnier, O. & Etoubleau, J. 1999. The age and distribution of mantle heterogeneity along the Mid-Atlantic Ridge (31–41°N). *Earth planet. Sci. Lett.,* **170**(3), 269–286.

Dziewonski, A., Bloch, S. & Landisman, M. 1969. A technique for the analysis of transient seismic signals. *Bull. seism. Soc. Am.,* **59**(1), 427–444.

Dziewonski, A., Hales, A. & Lapwood, E. 1975. Parametrically simple earth models consistent with geophysical data. *Phys. Earth planet Inter.,* **10**(1), 12–48.

Fernandes, R.M., Ambrosius, B.A., Noomen, R., Bastos, L., Wortel, M.J., Spakman, W. & Govers, R. 2003. The relative motion between Africa and Eurasia as derived from ITRF2000 and GPS data. *Geophys. Res. Lett.,* **30**(16), 1–5.

Fernandes, R.M., Bastos, L., Miranda, J.M., Lourenço, N., Ambrosius, B.A., Noomen, R. & Simons, W., 2006. Defining the plate boundaries in the Azores region, *J. Volcanol. Geotherm. Res,* **156**(1-2), 1–9.

Foster, A., Ekstrom, G. & Nettles, M. 2013. Surface wave phase velocities of the Western United States from a two-station method. *Geophys. J. Int.,* **196**(2), 1189–1206.

Gardiner, N.J., Johnson, T.E., Kirkland, C.L. & Szilas, K. 2019. Modelling the hafnium-neodymium evolution of early Earth: a study from West Greenland. *J. Petrol.,* **60**(1), 177–197.

Gente, P., Dyment, J., Maia, M. & Goslin, J. 2003. Interaction between the Mid-Atlantic Ridge and the Azores hot spot during the last 85 myr: emplacement and rifting of the hot spot-derived plateaus. *Geochem. Geophys. Geosyst.,* **4**(10), https://doi.org/10.1029/2003GC000527.

Goldstein, P. & Snoke, A. 2005. *SAC Availability for the IRIS Community,* Incorporated Institutions for Seismology Data Management Center Electronic Newsletter.

Grevemeyer, I., Ranero, C.R. & Ivandic, M. 2018. Structure of oceanic crust and serpentinization at subduction trenches. *Geosphere,* **14**(2), 395–418.

Hannemann, K., Krüger, F. & Dahm, T. 2013. Measuring of clock drift rates and static time offsets of ocean bottom stations by means of ambient noise. *Geophys. J. Int.,* **196**(2), 1034–1042.

Hannemann, K., Krüger, F., Dahm, T. & Lange, D. 2016. Oceanic lithospheric S-wave velocities from the analysis of P-wave polarization at the ocean floor. *Geophys. J. Int.,* **207**(3), 1796–1817.

Hannemann, K., Krüger, F., Dahm, T. & Lange, D. 2017. Structure of the oceanic lithosphere and upper mantle north of the Gloria Fault in the eastern mid-Atlantic by receiver function analysis. *J. geophys. Res. Solid Earth,* **122**(10), 7927–7950.

Harmon, N., Forsyth, D. & Webb, S. 2007. Using ambient seismic noise to determine short-period phase velocities and shallow shear velocities in young oceanic lithosphere. *Bull. seism. Soc. Am.,* **97**(6), 2009–2023.

Herrmann, R.B. 2013. Computer programs in seismology: an evolving tool for instruction and research. *Seismol. Res. Lett.,* **84**(6), 1081–1088.

Herrmann, R.B. & Ammon, C.J. 2002. Surface waves, receiver functions and crustal structure, in *Computer Programs in Seismology,* Saint Luis University, pp. 133–135.

Kamiya, S. & Kobayashi, Y. 2000). Seismological evidence for the existence of serpentinized wedge mantle. *Geophys. Res. Lett.,* **27**(6), 819–822.

Kelemen, P.B., Shimizu, N. & Salters, V.J. 1995. Extraction of mid-ocean-ridge basalt from the upwelling mantle by focused flow of melt in dunite channels. *Nature,* **375**(6534), 747–753.

Köhler, A., Weidle, C. & Maupin, V. 2012. On the effect of topography on surface wave propagation in the ambient noise frequency range. *J. Seismol.,* **16**(2), 221–231.

Krüger, F., Dahm, T. & Hannemann, K. 2020. Mapping of Eastern North Atlantic Ocean seismicity from Po/So observations at a mid-aperture seismological broad-band deep sea array. *Geophys. J. Int.,* **221**(2), 1055–1080.

Laske, G., Masters, G., Ma, Z. & Pasyanos, M. 2013. *Update on CRUST1.0 - A 1-degree Global Model of Earth´s Crust,* in: *Geophys. Res. Abstr,* p.2658.

Levshin, A.L. & Ritzwoller, M.H. 2001. Automated detection, extraction, and measurement of regional surface waves. *Pure appl. Geophys.,* **158**(8), 1531–1545.

Lin, P.Y.P., Gaherty, J.B., Jin, G., Collins, J.A., Lizarralde, D., Evans, R.L. & Hirth, G. 2016. High-resolution seismic constraints on flow dynamics in the oceanic asthenosphere. *Nature,* **535**(7613), 538–541.

Liu, M., Gerya, T. & Rozel, A.B. 2022. Self-organization of magma supply controls crustal thickness variation and tectonic pattern along melt-poor mid-ocean ridges. *Earth planet. Sci. Lett.,* **584,** 117482, https://doi.org/10.1016/j.epsl.2022.117482.

Luis, J.F. & Miranda, J.M. 2008. Reevaluation of magnetic chrons in the North Atlantic between 35°N and 47°N: implications for the formation of the Azores Triple Junction and associated plateau. *J. geophys. Res. Solid Earth,* **113**(10), 1–12.

Madureira, P., Moreira, M., Mata, J. & Allègre, C.J. 2005. Primitive neon isotopes in Terceira Island (Azores archipelago). *Earth planet. Sci. Lett,* **233**(3-4), 429–440.

Madureira, P., Moreira, M., Mata, J., Nunes, J.C., Gautheron, C., Lourenço, N., Carvalho, R. & de Abreu, M.P. 2014. Helium isotope systematics in the vicinity of the Azores triple junction: constraints on the Azores geodynamics. *Chem. Geol.,* **372,** 62–71.

Meier, T., Dietrich, K., Stöckhert, B. & Harjes, H.P. 2004. One-dimensional models of shear wave velocity for the eastern Mediterranean obtained from the inversion of Rayleigh wave phase velocities and tectonic implications. *Geophys. J. Int.,* **156**(1), 45–58.

Moreira, M. & Allègre, C.-J. 2002. Rare gas systematics on Mid Atlantic Ridge (37–40° N). *Earth planet. Sci. Lett.,* **198**(3–4), 401–416.

Moreira, M.A., Madureira, P. & Mata, J. 2018. Noble gas constraints on the origin of the Azores Hotspot, in *Active Volcanoes of the World,* pp. 281–299, Springer Science and Business Media Deutschland GmbH. https://doi.org/10.1007/978-3-642-32226-6_12.

Müller, R.D., Sdrolias, M., Gaina, C. & Roest, W.R. 2008. Age, spreading rates, and spreading asymmetry of the world's ocean crust. *Geochem. Geophys. Geosyst.,* **9**(4), https://doi.org/10.1029/2007GC001743.

Niu, Y. & Hékinian, R. 1997. Spreading-rate dependence of the extent of mantle melting beneath ocean ridges. *Nature,* **385**(6614), 326–329.

Niu, Y.L. & Humphreys, E.R. 2009. On the origin of OIB and LVZ-some new perspectives. *Geochim. Cosmochim. Acta Suppl.,* **73,** A948.

Olive, J.-A. 2023. Mid-ocean ridges: geodynamics written in the seafloor, in *Dynamics of Plate Tectonics and Mantle Convection,* ed. Duarte, J. C., pp. 483–510. Elsevier, https://doi.org/10.1016/B978-0-323-85733-8.00018-4.

Pariso, J.E., Sempéré, J.-c. & Rommevaux, C. 1995. Temporal and spatial variations in crustal accretion along the Mid-Atlantic Ridge (29°-31°30 N) over the last 10 m.y.: implications from a three-dimensional gravity study. *J. geophys. Res. Solid Earth,* **100**(B9), 17781–17794.

Penrose Conference Participants. 1972. Penrose field conference on ophiolites. *Geotimes,,* **17**(12), 24–25.

Putirka, K. 2008. Excess temperatures at ocean islands: implications for mantle layering and convection. *Geology,* **36**(4), 283–286.

Raitt, R.W. 1963. The crustal rocks, in *The Sea,* Vol., **3,** pp. 85–102, ed. Hill, S. Wiley, New York.

Rawlinson, N. 2005. *FMST: Fast Marching Surface Tomography Package–Instructions,* Research School of Earth Sciences, Australian National University, Canberra, pp. 1–24.

Rawlinson, N., Reading, A.M. & Kennett, B.L.N. 2006. Lithospheric structure of Tasmania from a novel form of teleseismic tomography. *J. geophys. Res.: Solid Earth,* **111**(B2), https://doi.org/10.1029/2005JB003803.

Ribeiro, L.P., Martins, S., Hildenbrand, A., Madureira, P. & Mata, J. 2017. The genetic link between the Azores Archipelago and the Southern Azores Seamount Chain (SASC): the elemental, isotopic and chronological evidences. *Lithos,* **294-295,** 133–146.

Rospabé, M., Ceuleneer, G., Le Guluche, V., Benoit, M. & Kaczmarek, M.A. 2021. The chicken and egg dilemma linking dunites and chromitites in the mantle-crust transition zone beneath oceanic spreading centres: a case study of chromite-hosted silicate inclusions in dunites formed at the top of a mantle diapir (Oman Ophiolite). *J. Petrol.,* **62**(4), 1–27.

Rychert, C.A., Harmon, N., Constable, S. & Wang, S. 2020. The nature of the lithosphere-asthenosphere boundary. *J. geophys. Res.: Solid Earth,* **125**(10), https://doi.org/10.1029/2018JB016463.

Sato, Y. 1955. Analysis of dispersed surface waves by means of Fourier transform I, *Bull. Earthq. Res. Inst.,* **33,** 33–47, http://repository.dl.itc.u-tokyo.ac.jp/dspace/handle/2261/11797.

Schimmel, M., Stutzmann, E. & Gallart, J. 2011. Using instantaneous phase coherence for signal extraction from ambient noise data at a local to a global scale. *Geophys. J. Int.,* **184**(1), 494–506.

Scholz, C. 2002. Mechanics of faulting, in *The Mechanics of Earthquakes and Faulting*(pp. 101–178). Cambridge: Cambridge University Press.

Shapiro, N.M. & Campillo, M. 2004. Emergence of broadband Rayleigh waves from correlations of the ambient seismic noise. *Geophys. Res. Lett.,* **31**(7), 8–11.

Shillington, D.J., Minshull, T.A., Peirce, C. & O'Sullivan, J.M. 2008. P- and S-wave velocities of consolidated sediments from a seafloor seismic survey in the North Celtic Sea Basin, offshore Ireland. *Geophys. Prospect.,* **56**(2), 197–211.

Shinevar, W.J. *et al.* 2019. Causes of oceanic crustal thickness oscillations along a 74-M Mid-Atlantic Ridge Flow line. *Geochem. Geophys. Geosyst.,* **20**(12), 6123–6139.

Silveira, G., Stutzmann, E., Davaille, A., Montagner, J.P., Mendes-Victor, L. & Sebai, A. 2006. Azores hotspot signature in the upper mantle. *J. Volc. Geotherm. Res.,* **156**(1-2), 23–34.

Soomro, R.A., Weidle, C., Cristiano, L., Lebedev, S., Meier, T. & Working Group, P. 2016. Phase velocities of Rayleigh and Love waves in central and northern Europe from automated, broad-band, interstation measurements. *Geophys. J. Int.,* **204**(1), 517–534.

Tucholke, B.E., Lin, J., Kleinrock, M.C., Tivey, M.A., Reed, T.B., Goff, J. & Jaroslow, G.E. 1997. Segmentation and crustal structure of the western Mid-Atlantic Ridge flank, 25°25-27°10 N and 0-29 m.y., *J. geophys. Res. Solid Earth,* **102**(B5), 10203–10223.

Turcotte, D. & Schubert, G. 2014. *Geodynamics*(3rd edn). Cambridge: Cambridge University Press.

Udías, A., Arroyo, A. & Mezcua, J. 1976. Seismotectonic of the Azores-Alboran region. *Tectonophysics,* **31**(3-4), 259–289.

Vaddineni, V.A., Singh, S.C., Grevemeyer, I., Audhkhasi, P. & Papenberg, C. 2021. Evolution of the crustal and upper mantle seismic structure from 0–27 ma in the Equatorial Atlantic Ocean at 2° 43′S. *J. geophys. Res.: Solid Earth,* **126**(6), https://doi.org/10.1029/2020JB021390.

Wang, Q., Bagdassarov, N. & Ji, S. 2013. The Moho as a transition zone: a revisit from seismic and electrical properties of minerals and rocks. *Tectonophysics,* **609,** 395–422.

Wang, T., Lin, J., Tucholke, B. & Chen, Y.J. 2011. Crustal thickness anomalies in the North Atlantic Ocean basin from gravity analysis. *Geochem. Geophys. Geosyst.,* **12**(3). https://doi.org/10.1029/2010GC003402.

Wang, Z. & Singh, S.C. 2022. Seismic evidence for uniform crustal accretion along slow-spreading ridges in the equatorial Atlantic Ocean. *Nat. Commun.,* **13**(1), https://doi.org/10.1038/s41467-022-35459-z.

Wessel, P., Smith, W.H., Scharroo, R., Luis, J. & Wobbe, F. 2013. Generic mapping tools: improved version released. *Eos, Trans. Am. geophys. Un.,* **94**(45), 409–410.

White, R.S., McKenzie, D. & O'Nions, R.K. 1992. Oceanic crustal thickness from seismic measurements and rare earth element inversions. *J. geophys. Res.,* **97**(B13), 19683, doi:10.1029/92JB01749.

White, R.S., Minshull, T.A., Bickle, M.J. & Robinson, C.J. 2001. Melt generation at very slow-spreading oceanic ridges: constraints from geochemical and geophysical data. *J. Petrol.,* **42**(6), 1171–1196.

Yang, T., Shen, Y., van der Lee, S., Solomon, S.C. & Hung, S.H. 2006. Upper mantle structure beneath the Azores hotspot from finite-frequency seismic tomography. *Earth planet. Sci. Lett.,* **250**(1-2), 11–26.

Yao, H., Gouédard, P., Collins, J.A., McGuire, J.J. & van der Hilst, R.D. 2011. Structure of young East Pacific Rise lithosphere from ambient noise correlation analysis of fundamental- and higher-mode Scholte-Rayleigh waves. *C. R. Geosci.,* **343**(8-9), 571–583.

Zhang, H., Geissler, W.H., Schmidt-Aursch, M.C. & Bonadio, R. 2022. Crustal and uppermost mantle structure beneath Tristan da Cunha using surface wave phase velocity from horizontal components OBS ambient seismic noise. *Geophys. J. Int.,* **232**(2), 1276–1292.

Zhou, D., Li, C.F., Zlotnik, S. & Wang, J. 2020. Correlations between oceanic crustal thickness, melt volume, and spreading rate from global gravity observation. *Mar. Geophys. Res.,* **41**(3). https://doi.org/10.1007/s11001-020-09413-x.

Zimmer, M., Prasad, M. & Mavko, G. 2002. Pressure and porosity influences on VP−VS ratio in unconsolidated sands. *Leading Edge,* **21**(2), 178–183.